

Ultrasmall silicon nanoparticles as a promising platform for multimodal imaging

Singh, G.; Ddungu, J. L. Z.; Licciardello, N.; Bergmann, R.; de Cola, L.; Stephan, H.;

Originally published:

October 2019

Faraday Discussions 222(2020), 362-383

DOI: <https://doi.org/10.1039/C9FD00091G>

Perma-Link to Publication Repository of HZDR:

<https://www.hzdr.de/publications/Publ-29786>

Release of the secondary publication
on the basis of the German Copyright Law § 38 Section 4.

Ultrasmall silicon nanoparticles as a promising platform for multimodal imaging

Received 00th January 20xx,
Accepted 00th January 20xx

DOI: 10.1039/x0xx00000x

Garima Singh^a, John L. Z. Ddungu^{b,c}, Nadia Licciardello^{a#}, Ralf Bergmann^a, Luisa De Cola^{b,c*}, Holger Stephan^{a*}

Bimodal systems for nuclear and optical imaging are currently being intensively investigated due to their comparable detection sensitivity and complementary information they provide. In this perspective, we have implemented both modalities on biocompatible ultrasmall silicon nanoparticles (Si NPs). Such nanoparticles are particularly interesting since highly biocompatible, covalent surface functionalization and demonstrated a very fast body clearance. We prepared monodisperse citrate-stabilized Si NPs (2.4 ± 0.5 nm) with more than 40 accessible terminal amino groups per particle and, for the first time, simultaneously a near-infrared dye (IR800-CW) and a radiolabel (⁶⁴Cu-NOTA = 1,4,7-triazacyclononane-1,4,7-triacetic acid) have been covalently linked to the surface of such Si NPs. The obtained nanomaterials have been fully characterized them by HR-TEM, XPS, UV-Vis and FT-IR spectroscopy. These dual-labelled particles do not exhibit any cytotoxicity *in vitro*. *In vivo* studies employing both positron emission tomography (PET) and optical imaging (OI) techniques revealed a rapid renal clearance of dual-labelled Si NPs from mice.

Introduction

Molecular imaging is a non-invasive method that provides reliable information on anatomy, as well as physiological and pathophysiological processes in living systems. Various imaging modalities such as computed tomography (CT), magnetic resonance imaging (MRI), optical imaging (OI), single-photon emission computed tomography (SPECT) and positron emission tomography (PET) are available for this purpose.¹⁻⁷ Each imaging modality has its own unique strength and intrinsic limitations, mainly regarding spatial/depth resolution

and sensitivity, making the achievement of precise and reliable information at the disease site difficult. In order to circumvent the limitations of a single imaging technique and exploit their advantages synergistically, multimodal molecular imaging has recently gained importance. Of particular interest is the combination of nuclear and optical methods. In this respect, the use of PET due to its high specificity/sensitivity (fM to pM range) and the possibility of quantifying the data, and near infrared fluorescence imaging, which enables high resolution, relatively deep penetration (cm range) and the use of fluorescence-guided surgery is a winning combination.

^a Institute of Radiopharmaceutical Cancer Research, Helmholtz-Zentrum Dresden - Rossendorf, Bautzner Landstraße 400, Dresden, D-01328, Germany

^b Laboratoire de Chimie et des Biomatiériaux Supramoléculaires, Institut de Science et d'Ingénierie Supramoléculaires (ISIS), 8 allée Gaspard Monge, Strasbourg, 67000, France

^c Institut für Nanotechnologie (INT), Karlsruher Institut für Technologie (KIT) Campus North, Hermann-von-Helmholtz-Platz 1, Eggenstein-Leopoldshafen, 76344, Germany

Current address: International Iberian Nanotechnology Laboratory, Avenida Mestre José Veiga s/n, 4715-330 Braga, Portugal

Corresponding authors:

* Dr. Holger Stephan, Helmholtz-Zentrum Dresden - Rossendorf, Institute of Radiopharmaceutical Cancer Research, Bautzner Landstrasse 400, 01328 Dresden, Germany, Phone: +49 3512603091, Fax: +49 3512603232, E-Mail: h.stephan@hzdr.de

* Prof. Luisa De Cola, Laboratoire de Chimie et des Biomatiériaux Supramoléculaires, Institut de Science et d'Ingénierie Supramoléculaires (ISIS), 8 allée Gaspard Monge, Strasbourg, 67000, France, Phone: +33 368855220; Fax: +33 368855242, E-Mail: decola@unistra.fr

† Electronic Supplementary Information (ESI) available.

See DOI: 10.1039/x0xx00000x

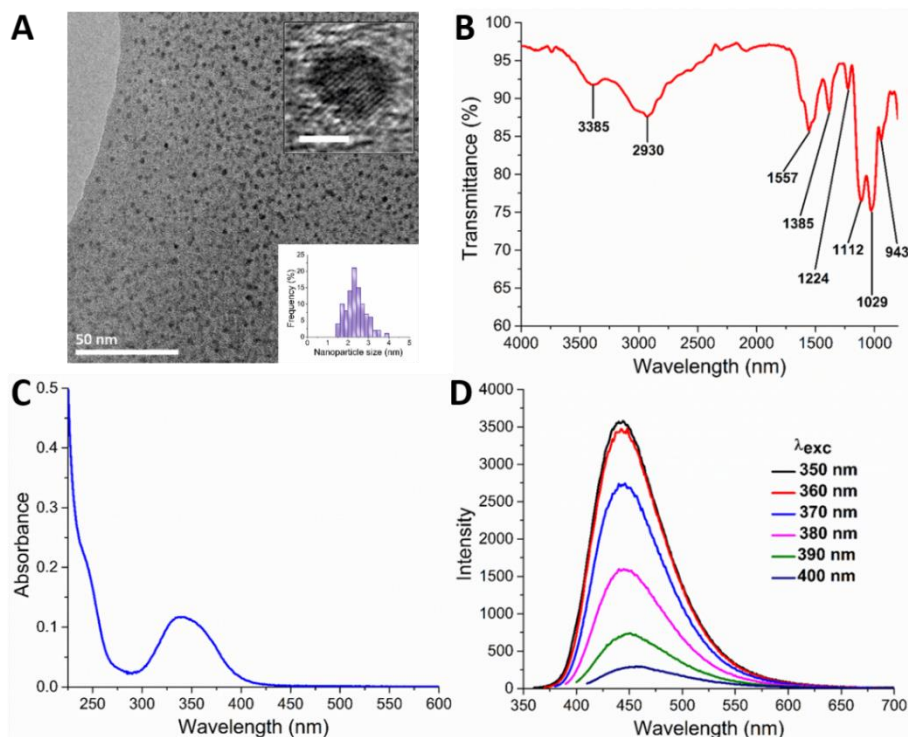
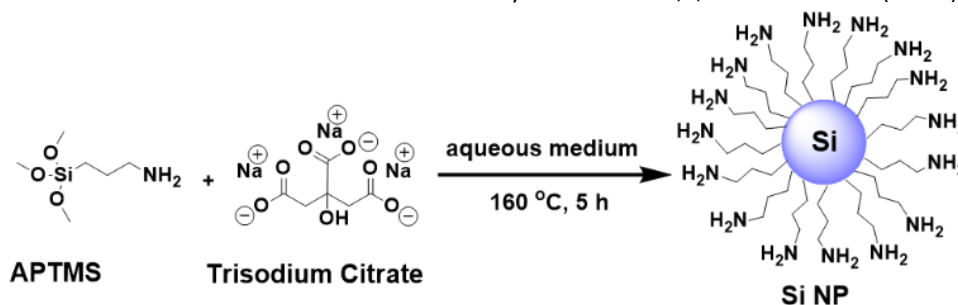


Fig. 1 Characterisation of Si NPs: A. TEM and HR TEM image (inset scale bar = 2 nm) with associated size distribution, B. FT-IR spectrum, C. UV-Vis absorption spectrum, D. Emission spectra.

Implementation of both modalities on the same system requires multifunctional molecules or nanomaterials. Due to their diverse modification possibilities, nanoscale materials have become significantly more important in recent years for imaging applications.⁸⁻¹⁶ This is due to the fact that it is possible to anchor a large number of similar or different modalities to a probe and thus increase the sensitivity on one hand and to follow *in vitro* and *in vivo* processes in more detail on the other. In addition, biological vector molecules can be introduced simultaneously for pharmaceutical targeting. For medical imaging however, very small materials that reach their target quickly and are renal excreted are desirable. The size considered optimal for such application is less than 6 nm, and particles with such small dimension are referred to as ultrasmall nanoparticles. Ultrasmall renal clearable nanoparticles possess enormous potential as cancer imaging agents¹⁷⁻²⁰, and in this respect biocompatible silicon nanoparticles (Si NPs) are highly attractive. Their covalent surface functionalization allows the introduction of different

labels for *in vivo* imaging.^{21,22} As far as biomedical applications are concerned, to date, Si NPs have been applied in bioimaging²³⁻²⁷ and in real-time immunofluorescence imaging.²⁸⁻³³ For instance, to target cells in a specific way, Si NPs have been successfully coupled with single-stranded DNA³⁴⁻³⁶, folic acid³⁷, sugars^{38,39}, peptides²⁹ and antibodies^{31,33}, and several *in vitro* studies have been performed on their cellular uptake⁴⁰⁻⁴² and cytotoxicity.⁴³⁻⁴⁵ *In vitro* investigations are mostly based on the intrinsic photoluminescence of the Si NPs. Through targeted surface modification, the luminescence properties can be tailored and, in particular, the quantum yield significantly increased.⁴⁶⁻⁵⁰

In contrast to *in vitro* studies, there are only a few *in vivo* studies with Si NPs so far using magnetic resonance and fluorescence imaging.^{37,51-55} For the first time, biodistribution and pharmacokinetic properties of radiolabelled Si NPs were reported by Kauzlarich *et al.*⁵⁶ Here, dextran-coated, manganese-doped, Si NPs were functionalized with a 1,4,7,10-tetraazacyclododecane-1,4,7-triacetic acid (DO3A) derivative



Scheme 1 Reaction scheme for the synthesis of amine-terminated Si NPs through the hydrothermal method [APTMS = (3-aminopropyl) trimethoxysilane].

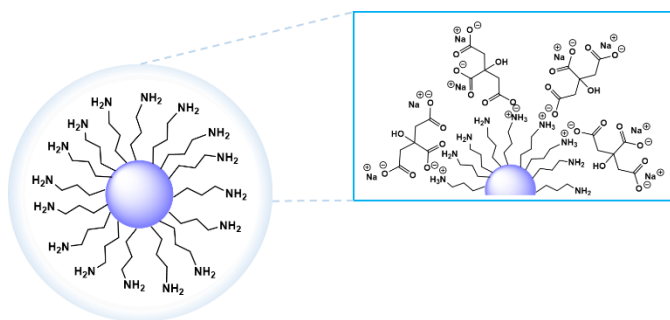
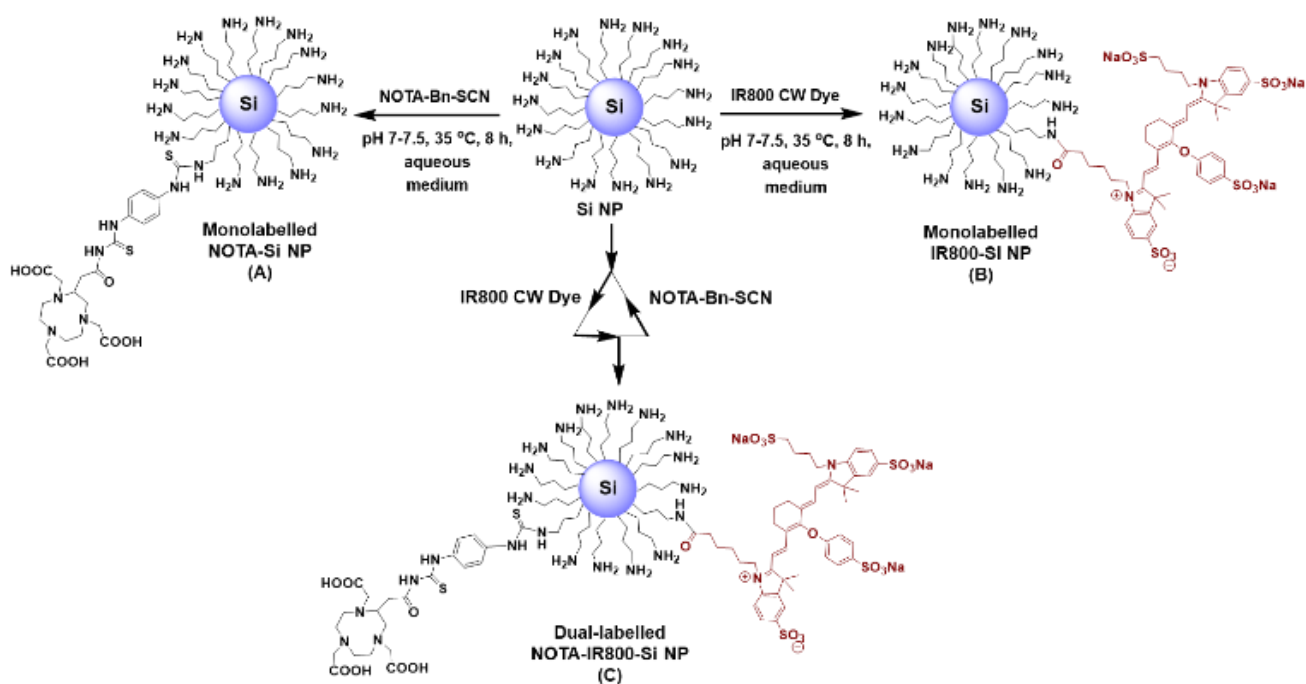


Fig. 2 Schematic representation of a Si-based nanoparticle surrounded by a “shell” of citric acid.

for labelling with ^{64}Cu , enabling PET studies. Owing to their relatively large hydrodynamic diameter (HD) (15.1 ± 7.6 nm), the particles have considerable liver uptake. Recently, we were able to show that ultrasmall ^{64}Cu -labelled Si NPs (size below 5 nm) are rapidly cleared from the body.⁵⁷ Despite the very small size, multiple and different functionalities can be grafted on the nanoparticle surface.

Based on our previous studies, we have selected citrate-stabilized Si NPs for further functionalization. The concurrent use of the bifunctional chelating agent NOTA (1,4,7-triazacyclononane-triacetic acid) and a near-infrared dye (IR800-CW) allows detailed *in vivo* studies using PET and optical imaging in small animals. Herein, we describe the synthesis of these dual-labelled particles, together with absorption, emission and structural properties. Subsequent assessment of nanotoxicity, as well as radiolabelling of Si NPs using the PET radionuclide ^{64}Cu is also reported in detail.

Results and Discussion



Scheme 2 Synthesis of NOTA-Si NPs (A), IR800-Si NPs (B) and NOTA-IR800-Si NPs (C).

Synthesis and characterisation of silicon-based nanoparticles

Water-dispersible amine-terminated silicon-based nanoparticles (Si NPs) were synthesised in hydrothermal conditions following our previously reported method.⁵⁷ A general synthetic route is depicted in **Scheme 1**. A broad characterisation of the Si NPs covering size, chemical composition and photoluminescence was carried out using a number of analytical techniques to show that the particles are completely comparable with our previous published work.⁵⁷

Observing the Si NPs through Transmission Electron Microscopy (TEM) (**Fig. 1A**) revealed a system of low polydispersity with an average size of 2.4 ± 0.5 nm. This smaller size of Si NPs compared to those achieved in our previous study⁵⁷ was achieved through optimisation of the synthetic procedure. Increasing the mixing time of the reagents from a total of 30 min to 60 min before heating in the oven affords a much more effective dispersion of the reagents during the hydrothermal process, creating more nuclei from which Si NPs can grow. A similar hypothesis has been reported for other species of silicon-based nanoparticles.⁵⁸

The pristine amine-terminated Si NPs exhibit a near neutral surface charge due to the formation of a stable citrate shell confirmed by DLS measurements (zeta potential ζ -5.3 ± 2.8 mV). More information on the surface structure of Si NPs was elucidated through FT-IR spectroscopy (**Fig. 1B**). Notable are bands occurring at 1557 cm^{-1} and 1385 cm^{-1} for symmetric and asymmetric vibrational modes of C=O bonds respectively, as well as a band at 1224 cm^{-1} originating from stretching of C—O bonds. These are assumed to be due to the presence of residual citric acid in the system as result of an interaction with the protonated amines on the Si NPs, confirming the expected structure, as reported in our previous work.⁵⁷

This presence of citric acid can be further identified by X-ray Photoelectron spectroscopy (XPS). Deconvolution of the high

resolution carbon scan (ESI Fig. S1/Table S1) shows a component with a binding energy of 287.6 eV, indicating the presence of oxygen bound carbon with sp^2 hybridisation. This is in addition to a major component with a binding energy of 285.8 eV, corresponding to oxygen bound carbon with sp^3 hybridisation. Taking the presence of both binding environments into account, it can be assumed that citric acid forms a "shell" of sorts around the Si NP through interactions with the surface amine groups as illustrated in Fig. 2. This was indeed already suggested in our previous work through NMR studies.⁵⁷ The UV-Vis absorption spectrum of the Si NPs was acquired in order to verify the similarity of the new batch to our previous work⁵⁷ and to compare to the literature.³³ As shown in Fig. 1C, the spectrum appears almost identical to those reported previously, with an absorption band observed at 340 nm. The emission spectra of the Si NPs are shown in Fig. 1D. An emission maximum is centred at about 450 nm for each excitation wavelength from 350 to 400 nm, matching the stable photoluminescence characteristics in the blue region as reported in the literature.^{33, 57} The emission quantum yield for these NPs is 15% in water. The surface amine groups were quantified and the average concentration was estimated to be 4.16 $\mu\text{mol NH}_2$ per mg Si NPs which was used to calculate a value of approximately 43 amine groups per particle (ESI Scheme S1/Fig. S2/Table S2/Equations S1, S2).

Table 1 Summary of characteristic features of NOTA-Si NPs, IR800-Si NPs and NOTA-IR800-Si NPs.

	NOTA-Si NPs	IR800-Si NPs	NOTA-IR800-Si NPs
IR800 conjugation (per mg Si NP conjugate)	-	0.013 μmol	0.010 μmol
NOTA conjugation (per mg Si NP conjugate)	0.090 μmol	-	0.091 μmol
Distribution coefficient (Log $D_{7.4}$)	-4.12 \pm 0.04	-	-3.84 \pm 0.10

Synthesis and characterisation of Si NPs conjugates NOTA-Si NPs, IR800-Si NPs and NOTA-IR800-Si NPs

The NOTA-Si NPs, as reported⁵⁷, were prepared by reacting amine-terminated Si NPs to NOTA-Bn-SCN (0.1 μmol per mg Si NP) and were purified by dialysis (MWCO: 1 kDa) against water (Scheme 2A). The reaction of the Si NPs with NHS-activated IR800 dye (0.5 μmol per mg Si NP), on the other hand, produced IR800-Si NPs (Scheme 2B). The near-infrared dye CW800 was employed for this modification because its emission wavelength (λ_{em} 789 nm) does not overlap with the auto-fluorescence of the biological tissues and thus, provides the necessary penetration depth for *in vivo* studies.^{59, 60} The IR800-Si NPs were purified by dialysis (MWCO: 3.5–5 kDa), followed by size exclusion chromatography (SEC) using Sephadex G-25. Dual-labelled NOTA-IR800-Si NPs were synthesized by sequential addition method where activated IR800 dye (0.5 μmol per mg Si NP) and NOTA-Bn-SCN (0.1 μmol per mg Si NP) were added sequentially in small amounts to the

aqueous Si NP solution over a period of 1 h (Scheme 2C). It is worth mentioning that simultaneous addition of NOTA and IR800 led to non-uniform surface modifications of Si NPs, which could not be applied for dual imaging. The crude reaction mixture was also purified by dialysis (MWCO: 3.5–5 kDa) and SEC. The purity of the IR800-Si NPs and NOTA-IR800-Si NPs was verified by fluorescence (reverse phase thin layer chromatography RP-TLC) and radiolabelling (Radio-instant thin layer chromatography Radio-iTLC) studies (ESI Fig. S3).

Table 2 Comparative analysis of photophysical properties of mono-labelled vs dual-labelled Si NPs.

	IR800 dye	Si NPs	IR800-Si NPs	NOTA-IR800-Si NPs
Max. absorbance λ_{abs}	775 nm	355 nm	612 nm	611 nm
Max. fluorescence λ_{em}	792 nm	456 nm	754 nm	748 nm
λ_{exc}	775 nm	360 nm	611 nm	611 nm
PLQY	14.2%	15%	22.5%	15.7%

The zeta potential of both the unimodal (NOTA-Si NPs and IR800-Si NPs: -5.4 ± 4.1 mV) and the bimodal particles (NOTA-IR800-Si NPs: -5.1 mV \pm 3.5 mV) is in the same range as that of the pristine particles.

The hydrophilicities of [^{64}Cu]Cu-NOTA-Si NPs and [^{64}Cu]Cu-NOTA-IR800-Si NPs were determined by 1-octanol/water distribution experiments to predict the behaviour of the conjugates under physiological conditions. A log $D_{7.4}$ value of -4.12 ± 0.04 was obtained for [^{64}Cu]Cu-NOTA-Si NPs and -3.84 ± 0.10 for [^{64}Cu]Cu-NOTA-IR800-Si NPs. The slight increase in the distribution ratio of bimodal Si NPs is attributed to the presence additional IR800 dye. The negative distribution coefficients indicate the hydrophilic character of the Si NPs, which is a prerequisite for the rapid clearance of the particles *via* the renal pathway.

Radiometric and UV-Vis titrations were performed to quantify the amounts of NOTA and IR800 dye molecules present on the surface of modified Si NPs. Demanding only nanograms of the sample, the assays effectively derive the quantified value along with the purity of the conjugates.

Radiometric assay employed a mixture of radioactive ([^{64}Cu]CuCl₂) and non-radioactive copper (CuSO₄)⁶¹ at different concentrations to determine the amount of NOTA on the surface of Si NPs. The values were calculated to be ~ 0.090 μmol NOTA per mg NOTA-Si NP and ~ 0.091 μmol NOTA per mg NOTA-IR800-Si NP (ESI Fig. S4).

The amount of conjugated IR800 dye was determined by UV-Vis analysis based on Beer-Lambert's Law. The results reveal values of ~ 0.013 μmol IR800 per mg IR800-Si NP and ~ 0.010 μmol IR800 per mg NOTA-IR800-Si NP. The slight deviation in the quantities for unimodal and bimodal Si NPs features the additional NOTA present on the surface of NOTA-IR800-Si NPs (ESI Fig. S5).

The synthetic routes applied lead to Si NPs with defined amounts of NOTA and IR800 molecules, allowing the

simultaneous application of PET and OI after an appropriate radiolabelling of the particles. A summary of physicochemical properties of the mono and dual-labelled Si NPs is presented in **Table 1**.

Absorption and emission properties of IR800-Si NPs and NOTA-IR800-Si NPs

The maximum absorbance for IR800-Si NPs is observed at λ_{abs} 611 nm, which portrays a huge hypsochromic shift, compared to absorbance of the IR800 dye (λ_{abs} 775 nm) (**Fig. 3A**). The probable reason for this massive shift and the profile broadening of the absorbance peak could be due to the formation of H-aggregates, as observed for other cyanine dyes in the presence of protonated amines, or their interaction with the surface.^{62, 63} Nonetheless, the IR800-Si NPs remain in the NIR region (600–900 nm) and thus, are applicable for *in vivo* trials as potential imaging agents. The emission band of the IR800-Si NPs is observed at λ_{em} 753 nm (λ_{exc} 611 nm) which also depicts a small blue shift compared to the free dye (IR800 dye λ_{em} 792 nm, λ_{exc} 775 nm).

The absorbance maxima for dual-labelled NOTA-IR800-Si NPs is also depicted at λ_{abs} 611 nm with a typical cyanine shoulder at 470 nm, which confirms the conjugation of the IR800 dye to the Si NPs. The maximum emission on the other hand, for NOTA-IR800-Si NPs is observed at λ_{em} 748 nm (λ_{exc} 611 nm). A comparative UV-Vis and fluorescence spectra of IR800-Si NPs and NOTA-IR800-Si NPs is shown in **Fig. 3B**. The photoluminescent quantum yield (PLQY) for IR800-Si NPs (22.5%) is reported to be higher compared to that of dual-labelled NOTA-IR800-NOTA (15.7%) and the IR800 dye

(14.2%).⁶⁴ **Table 2** summarizes the photophysical properties of the Si NPs and its derivatives.

Radiolabelling studies of NOTA-Si NPs and NOTA-IR800-Si NPs

The radiolabelling experiments were carried out according to our reported protocol for ⁶⁴Cu-labelling.⁵⁷ In brief, NOTA-Si NPs and NOTA-IR800-Si NPs were labelled with [⁶⁴Cu]CuCl₂ radionuclide at pH 6 (MES/NaOH buffer) at room temperature for 30 min. [⁶⁴Cu]Cu-NOTA-Si NPs and [⁶⁴Cu]Cu-NOTA-IR800-Si NPs were obtained in > 90% radiochemical yields (RCY) with a specific activity of ~3 MBq and ~2 MBq per 100 μ g Si NP conjugates determined by Radio-iTLC. Variation in the parameters, such as increasing the reaction time and slight elevation of the temperature did not notably affect the radiolabelling of the Si NP conjugates. The radiolabelled Si NPs were purified by SEC to obtain ~98% radiochemical purity. Challenge experiments were performed using a 10,000 fold excess of EDTA for 24 h with no indication of transchelation.

Nanotoxicity of NOTA-Si NPs, IR800-Si NPs and NOTA-IR800-Si NPs

For nano-objects to be developed for pre-clinical and clinical imaging trials, it is of the utmost importance to evaluate their integrity and biocompatibility. Our previous studies with citrate-stabilized Si NPs equipped with NOTA revealed that these particles have a very low, if any, cytotoxicity in a human embryonic kidney (HEK 293) cell line.⁵⁷ This is in accordance with results obtained with similar silicon particles in other cell lines, *i.e.*, HeLa, HepG2, Caco-2 and CCD-841.^{33, 65, 66}

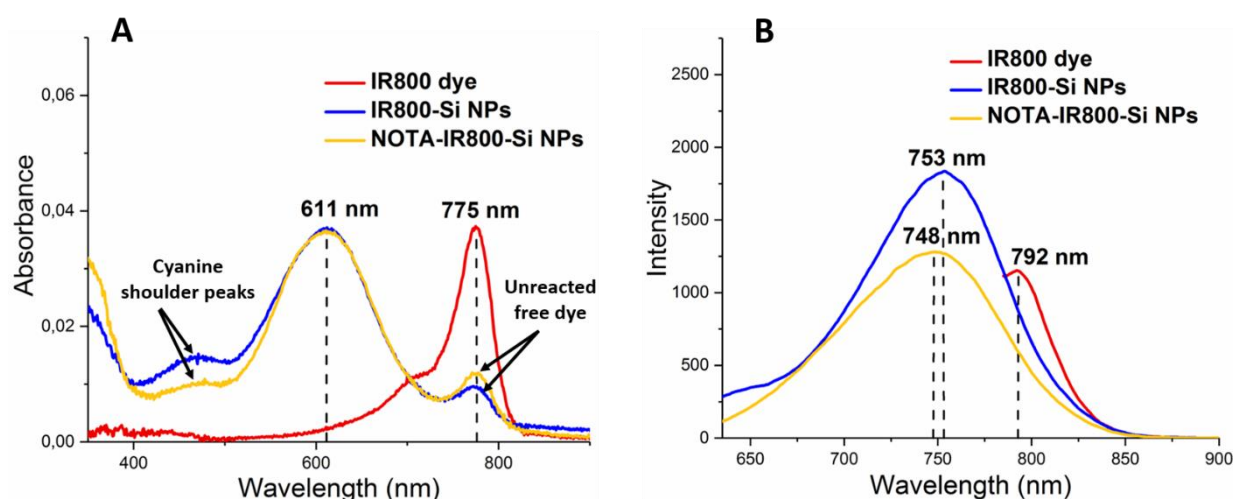


Fig. 3 Comparative absorption (A) and emission (B) spectra of IR800-Si NPs, NOTA-IR800-Si NPs and IR800 dye in water (IR800-Si NPs and NOTA-IR800-Si NPs λ_{exc} 611 nm; IR800 dye λ_{exc} 775 nm).

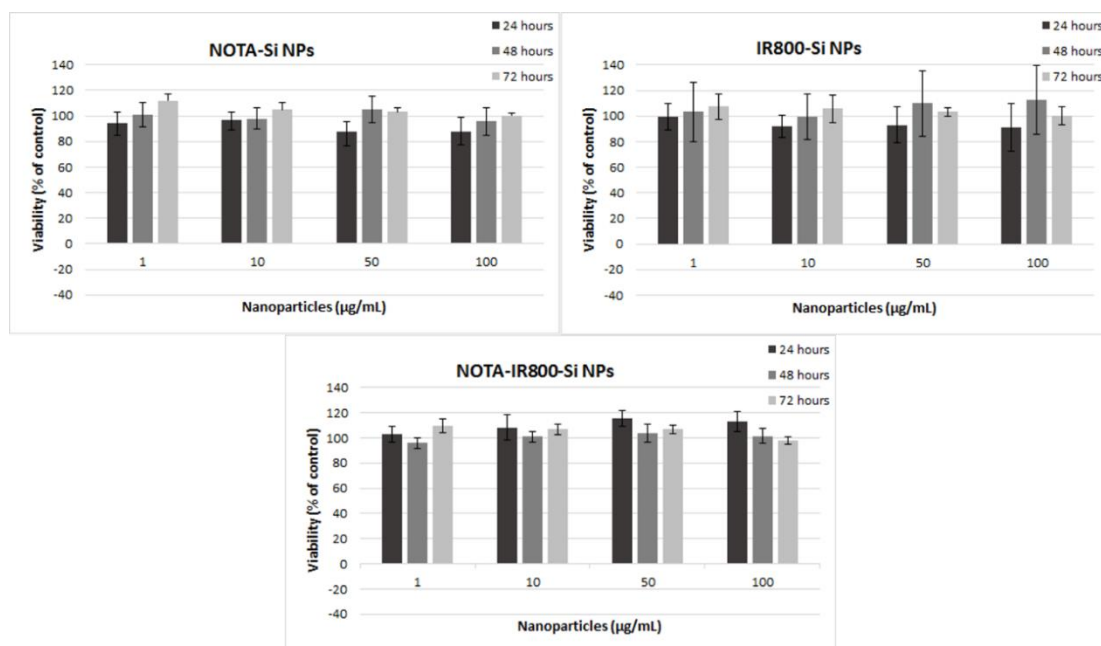


Fig. 4 Effect of NOTA-Si NPs, IR800-Si NPs and NOTA-IR800-Si NPs on the viability of HEK293 cells. The cells were exposed to 1, 10, 50 and 100 $\mu\text{g/mL}$ Si NPs dispersions for 24, 48 and 72 h respectively in Dulbecco's modified eagle's medium (DMEM) supplemented with 10% fetal bovine (FBS) and viability was determined using CyQuant assay.

The current renal clearable particles NOTA-Si NPs, IR800-Si NPs and NOTA-IR800-Si NPs were tested in HEK293 kidney cells utilising MTS ([3-(4,5-dimethylthiazol-2-yl)-5-(3-carboxymethoxyphenyl)-2-(4-sulfophenyl)-2H-tetrazolium]), LDH (lactate dehydrogenase) and CyQuant assays to assess their *in vitro* behaviour. For the cell viability and cytotoxicity measurements, the HEK293 cells were incubated with 1, 10, 50 and 100 $\mu\text{g/mL}$ Si NP conjugates and analyzed after 24, 48 and 72 hours. The MTS assay determines the number of viable cells. The LDH cytotoxicity assay investigates the amount of released lactate dehydrogenase from damaged cells and thus provides information whether the cell membrane is intact. The results obtained using MTS and LDH assays are summarized in **ESI (Figs. S6-S7)**. Negligible effects of NOTA-Si NPs, IR800-Si NPs and NOTA-IR800-Si NPs on cell metabolism, viability and integrity were observed for HEK293 cells. In addition, we performed the cell proliferation assay CyQuant. This fluorescence-based assay detects the viable cellular DNA. As

shown in **Fig. 4**, cell viability was not affected for all the three kinds of Si NPs at all concentrations even after 72 h of incubation.

The results clearly show that the investigated particles do not have any cytotoxic effects. This is an important prerequisite for further *in vivo* investigations with regard to the biodistribution and pharmacokinetic properties.

Fluorescence imaging of IR800-Si NPs in healthy mice

For the biodistribution studies, ~ 100 μg of the IR800-Si NPs were administered intravenously in healthy mice ($n = 4$) which were analyzed at different time points (1 min, 10 min and 2 h) by whole body fluorescence scanners to detect the fluorescence intensity in each organ. Exemplary images of the mice at different time points are displayed in **Fig. 5A**. The fluorescence image 1 min *p.i.* projects a uniform distribution of the IR800-Si NP all over the body *via* blood circulation. Within 10 min the particles start to pass through the kidneys, towards

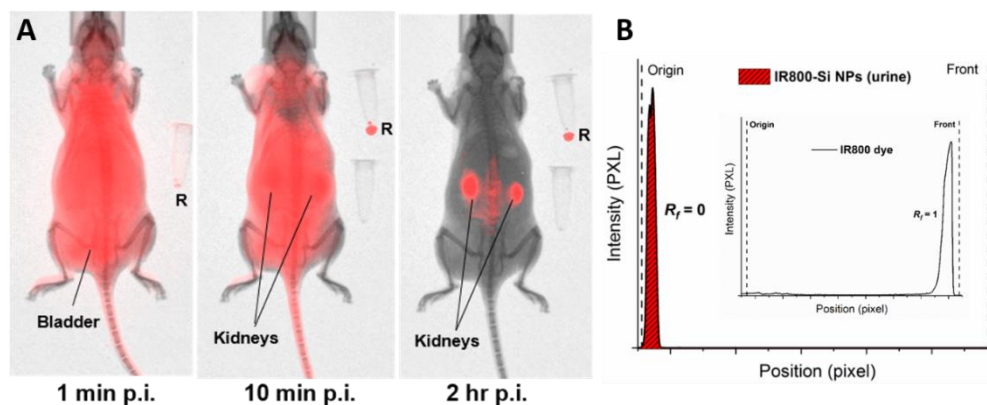


Fig. 5 A) *In vivo* optical imaging scans of IR800-Si NPs 1 min, 10 min and 2 h *p.i.* intravenously injected in healthy nu/nu mice. (R: injected IR800-Si NPs as reference). B) RP-TLC analysis of urine from experimental healthy mice 1 h *p.i.* of IR800-Si NP (IR800 dye inset); TLC system: RP-TLC plates, Solvent system: Methanol.

the bladder and are eventually eliminated *via* urine. The later time point (2 hours *p.i.*) depicts that the majority of IR800-Si NPs had already been excreted from the body with traces of fluorescence observed in the kidneys, visualized only with high intensity projections. In order to provide information on *in vivo* stability of IR800-Si NPs, urine from the mice was collected and analyzed (1 h *p.i.*). The RP-TLC displayed a single peak at the origin corresponding to the IR800-Si NPs ($R_f = 0$), and no free/detached fluorescence (IR800 dye, $R_f = 1$) was observed at the solvent front (Fig. 5B). This concludes that the nanoparticle conjugates were rapidly eliminated from the *in vivo* system *via* the renal pathway and confirms the integrity of the IR800-Si NPs in presence of complex biological milieu.

chromatograms of injected Si NPs and the urine samples correspond to bimodal Si NPs ($R_f = 0$) and hence, confirms the *in vivo* integrity of the Si NPs.

PET imaging of dual-labelled [^{64}Cu]Cu-NOTA-IR800-Si NPs in NMRI nu/nu mice

In addition to the biodistribution studies, dynamic PET was carried out. [^{64}Cu]Cu-NOTA-IR800-Si NPs were injected intravenously (~ 10 MBq each) into mice ($n = 4$) and the whole body PET scans were recorded over 1 h. Exemplary figures of mid-frame time points at 5 min, 20 min, 30 min and 60 min are summarized in Fig. 8 to show fast clearance of the radiolabelled Si NPs from the kidneys into the urinary bladder. Within the first 5–10 minutes the bimodal Si NPs distribute

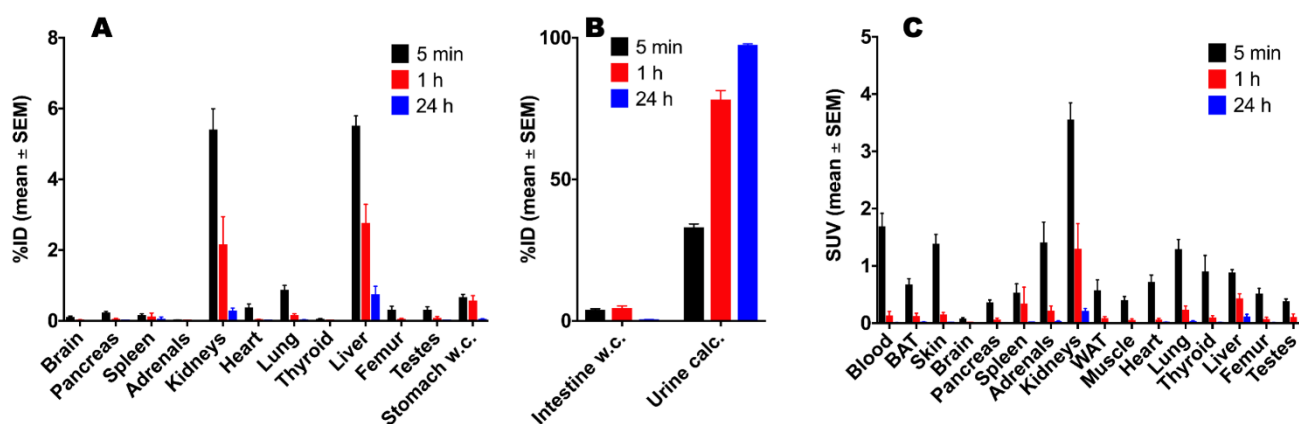


Fig. 7 Biodistribution of [^{64}Cu]Cu-NOTA-IR800-Si NPs in NMRI nu/nu mice at 5 min, 1 h and 24 h *p.i.* in extracted organs and tissues. A) %ID in selected organs, B) Eliminated activity in the intestine and urine (w.c.: with content), C) Activity concentrations (SUV) of selected organs and tissues. (BAT brown adipose tissue, WAT white adipose tissue).

Biodistribution of [^{64}Cu]Cu-NOTA-IR800-Si NPs in healthy mice

To study the biodistribution of dual labelled [^{64}Cu]Cu-NOTA-IR800-Si NPs, they were intravenously injected to non-anesthetised healthy nu/nu mice ($n = 5$). Selected organs and tissues of mice were excised 5 min, 1 h and 24 h *p.i.* for activity measurements. The amount of activity in the complete organs were calculated as % injected dose (%ID) and the activity concentrations in the organs and tissues were normalized to the body weight ($\text{SUV} = \text{activity concentration in the tissue/injected activity} \times \text{body weight}$). These values were evaluated to define the biodistribution and mode of elimination of the dual mode Si NPs. The biodistribution studies depicted the elimination of 30% [^{64}Cu]Cu-NOTA-IR800-Si NPs *via* urine from kidneys 5 min *p.i.*, which spiked to 75% at 1 h and 100% after 24 h (Figs. 6A,B). Minor amounts of activity ($< 5\%$ ID) were detected 1 hour *p.i.* in the liver, intestine and other organs/tissues. The normalized SUV values give a better overview about the biodistribution of the Si NPs with negligible activity in the whole body, particularly in kidneys and liver after 24 h (Fig. 6C). The results confirmed the extremely fast and complete renal clearance of these hydrophilic Si NPs from the *in vivo* system.

The largest activity amount was found in the urine. Therefore, the urine from the experimental mice was collected 5 min and 1 h *p.i.* and examined by Radio-iTLC (Fig. 7). The TLC

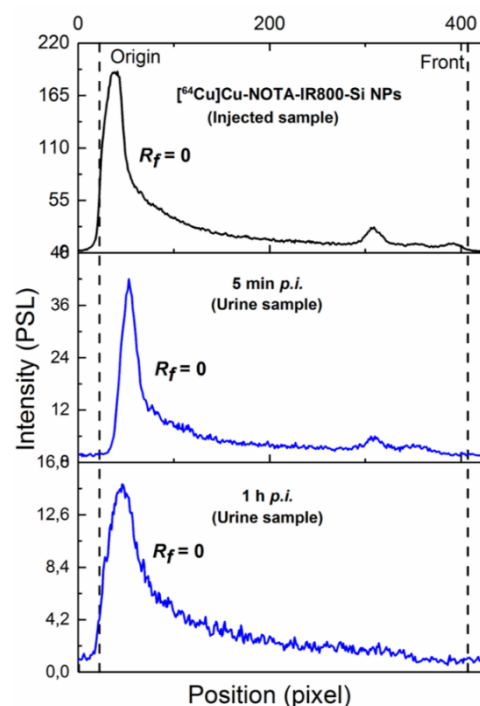


Fig. 6 Radio-iTLC of the injected and urine samples of [^{64}Cu]Cu-NOTA-IR800-Si NPs injected mice (5 min and 1 h *p.i.*). TLC system: Radio-iTLC plates, 2M NH_4OAc : MeOH (1:1, v:v), [^{64}Cu]Cu-NOTA-IR800-Si NPs $R_f = 0$.

uniformly in the whole body and then start eliminating *via* the kidneys. The particles show no signs of sticking in the renal medulla and easily pass through the glomerular pores within 1 h. The activity was temporarily retained only in the kidney pelvis from where it was excreted into the bladder.

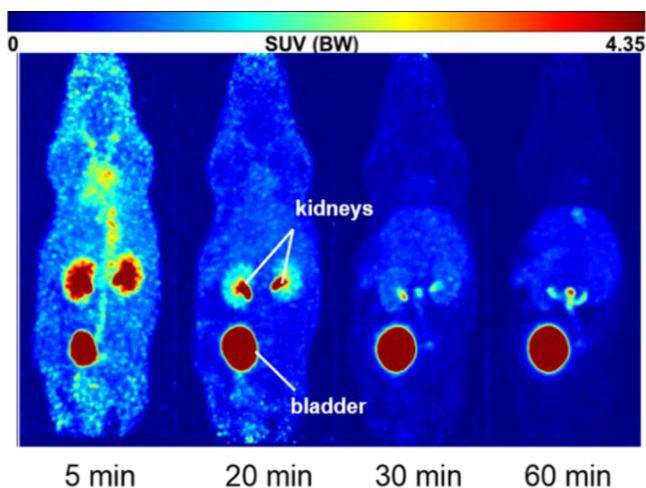


Fig. 9 *In vivo* PET imaging of $[^{64}\text{Cu}]\text{Cu-NOTA-IR800-Si}$ NPs 5, 20, 30, 60 min *p.i.*

Comparative nuclear and optical imaging of $[^{64}\text{Cu}]\text{Cu-NOTA-IR800-Si}$ NPs in healthy mice

The $[^{64}\text{Cu}]\text{Cu-NOTA-IR800-Si}$ NPs were not only examined by PET but also by fluorescence imaging (Fig. 9). For this purpose, one mouse was sacrificed 1 h after injection of the NPs. PET/CT and planar X-Ray 2D measurements of the mouse were recorded in prone and supine positions for detection of ^{64}Cu -activity and the fluorescence signal distribution in the body. All three imaging modalities revealed that within 1 h, the majority of the dual-labelled Si NPs remained in the kidneys and large amounts were excreted into the bladder. The higher kidney retention for this mouse in comparison to the previous PET study (see Fig. 8) can be attributed to a biological variation of

this mouse, *i.e.*, different reaction to anaesthesia and hydration of the animal. However, in accordance with the other experiments, the activity and fluorescence images detect only traces of activity and fluorescence in other organs. The PET shows small amounts in the gall bladder. This is another indication of the high metabolic stability of the dual-labelled NPs.

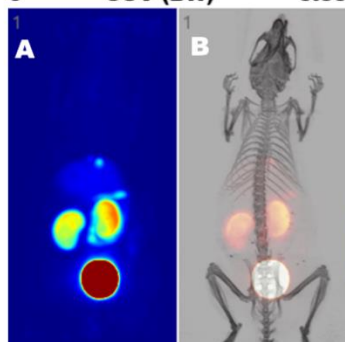
The complementary biocompatibility and rapid renal clearance of the NOTA-IR800-Si NPs deciphered by biodistribution, PET and optical imaging, confirms the bimodality of the Si NP system. The results also displayed excellent pharmacokinetics and extraordinary biocompatibility of the system, which is prerequisite for any nanoparticle platform adapted for *in vivo* studies. The most acceptable reason for this behaviour is the minimum required surface modification performed on the Si NP surface to achieve the imaging goals without hampering the size and surface charge of the particles.

Conclusions

In summary, ultrasmall amine-terminated Si NPs, prepared by hydrothermal synthesis, were equipped with the near-infrared dye IR800 and the bifunctional chelating agent NOTA to obtain a dual imaging probe. The subsequent *in vivo* investigations based on PET and OI show that these multifunctional particles are cleared very quickly *via* the kidneys and that the particles remain intact after excretion. The minimal, if any, cytotoxicity and *in vivo* integrity, as well as the favourable pharmacokinetic properties, underline the suitability of the NOTA-IR800-Si NPs for *in vivo* applications. Overall, these particles thus represent a promising platform for targeted multimodal imaging. Despite the very small size, several small targeting vector molecules such as peptides can be grafted on the nanoparticle surface. However, it must be ensured that size and charge of the particles are changed only minimally in order to maintain rapid circulation in the bloodstream and full clearance.

Maximum Intensity Projection

PET CT + PET
0 SUV (BW) 5.33



Radioactivity

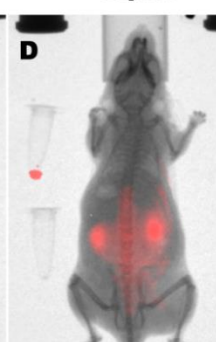
supine



2D Images

Fluorescence

supine



Radioactivity

prone



Fluorescence

prone

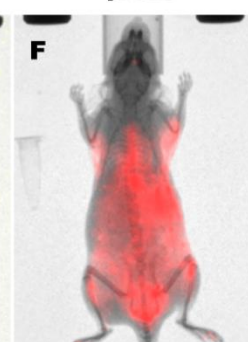


Fig. 8 Biodistribution of $[^{64}\text{Cu}]\text{Cu-NOTA-IR800-Si}$ NPs 1 h after single intravenous injection in an gas anesthetized NMRI nu/nu mouse. A) Maximum intensity projection (MIP) of the PET, B) the overlay of MIP with the X-ray tomogram, C) Planar 2D view of the activity distribution in supine position to the camera, D) Spectral unmixed fluorescence image, E) activity distribution in prone position, F) Fluorescence in prone position (Injected sample reference in Eppendorf tubes).

Experimental Methods and Materials

All chemicals were purchased from commercial suppliers and used as received without further purification. S-2-(4-Isothiocyanatobenzyl)-1,4,7-triazacyclononane-1,4,7-triacetic acid (SCN-Bn-NOTA; #B-605) was purchased from Macrocylics and the infrared dye 800CW from Li-COR biosciences. A Direct-Q 3 UV water purification system from Millipore (Merck KGaA) was applied for producing deionized water. The resistance of deionized water was 18.2 M Ω cm. Dialysis tubes were purchased from Serva (MWCO: 1 kDa and 3.5-5 kDa; Spectra/Por[®] 7 dialysis tubing); Sephadex G-25 desalting columns from GE healthcare. High pressure resistant home-made Teflon vessels (similar to those reported by Calzaferri et al.⁶⁷) were used for hydrothermal syntheses throughout this work.

Analysis, characterisation and purification techniques

TEM analysis was performed using a Jeol 2100F electron microscope operated at 200 kV. Samples were prepared by dispersing the aqueous suspensions of the Si NPs onto holey-carbon-on-copper grids (Quantifoil, GmbH) with the excess solvent evaporated. Hydrodynamic size and zeta potential measurement were performed using the dynamic light scattering (DLS) using Zetasizer NanoZS (Malvern Instruments, UK) with an angle detection of 173° at 25° C with a beam wavelength of 632.8 nm. Particle size determination as well as zeta potential measurements were conducted at a concentration of 2 mg/mL in 10 mM phosphate buffer saline (pH 7.4) in disposable plastic cuvettes with a square aperture (Malvern Instruments Ltd.). Prior to each experiment, the solutions were filtered through 0.02 μ m or 0.2 μ m syringe filters (GE Healthcare, Germany) and equilibrated for 2 mins. The stated value is a mean of three independent measurements. Zeta potential measurements were performed in a universal dip cell (Malvern Instruments Ltd.). The stated values are a mean of three independent measurements using the Smoluchowski model. Data were evaluated with Malvern Zetasizer Software 7.11 version. Ultraviolet-Visible absorption spectra for Si NPs were recorded on a Shimadzu UV-3600 double-beam UV-VIS-NIR spectrophotometer. Samples were measured using quartz cuvettes with a path length of 1 cm and volume of 3.5 mL. Absorption spectra for IR800-Si NPs and NOTA-IR800-Si NPs were conducted on Specord[®] S50 from Analytik Jena (Germany). The samples were measured on quartz micro cuvettes (d=1cm) with 400-500 μ L with a wavelength range from 190-1100 nm. The standard calibration curves and the molar extinction coefficient were calculated using the Beer-Lambert equation: $A = \epsilon \times l \times c$ where A is the absorbance at λ_{max} , ϵ denotes the extinction coefficient, c denotes the concentration and l denotes the path length of the cuvette (1 cm). For quantum yield experiments, the absorbance was kept between 0.01-0.1. The measurements were set relative to the blank solution (reference). Data were processed using the WinASPECT[®] software. For the Si NPs as synthesised and obtained after purification, steady-state emission spectra were recorded on a HORIBA Jobin-Yvon IBH

FL-322 Fluorolog 3 spectrometer equipped with a 450 W xenon arc lamp as the excitation source, double-grating excitation and emission monochromators (2.1 nm mm⁻¹ of dispersion; 1200 grooves mm⁻¹), and a TBX-04 single-photon-counting device as the detector. Emission and excitation spectra were corrected for source intensity (lamp and grating) and emission spectral response (detector and grating) by standard correction curves. Fluorescence emission measurements and quantum yield experiments for IR800-Si NPs and NOTA-IR800-Si NPs were done using an LS 55 (230V) luminescence spectrometer from PerkinElmer equipped with a xenon flash lamp source for excitation. Samples were measured in transparent disposable cuvettes of 2 mL with a wavelength range of 200-900 nm and the slit width of 10 nm. FL UV WinLab[®] software was used for Data analysis and acquisition. Fourier transform infrared (FTIR) spectra were recorded on a Shimadzu IRAffinity-1 spectrometer used in attenuated total reflectance (ATR) mode. Si NP samples were prepared by lyophilisation, with the resulting solids ground with an agate mortar and laid on the ATR crystal. Spectra cumulated 64 scans at a resolution of 4 cm⁻¹. Dialysis was performed on with regenerated cellulose membranes with ultra-pure cellulose ester Float-A-Lyzer membranes from Spectrum Labs, Germany with various molecular weight cut-off (MWCO: 1 kDa, 3.5-5 kDa) against water. Size Exclusion Chromatography was performed using PD-10 Desalting G25 column (Sephadex, G25 medium). The eluents used were Millipore water or 0.9% NaCl (wt/v) as indicated in the experiment section. Thin layer chromatography was conducted on reverse stationary phase silica gel using methanol as mobile phase systems in a vertical chamber for elution. UV lamp (254 nm) and Amersham Typhoon 5 Scanner (300-900 nm) were used for analysis of fluorescence labelled nanoparticles.

Synthesis of monomodal Si NP-based imaging agents

Si NPs: This procedure is taken and adapted from a previous report by He and coworkers.²⁸ 20 mL deionised H₂O was added to a 50 mL 2-neck flask. Argon gas was bubbled through the solution with stirring for 30 mins. Citric acid trisodium salt (0.83 g, 3.75 mmol) was added and stirring + bubbling of the mixture was continued for a further 30 mins. 3-aminopropyltrimethoxysilane (APTMS, 5 mL, 28.65 μ mol) was then added with continued stirring + bubbling and shortly after, the mixture was transferred to a Teflon pressure sealed vessel. Bubbling with argon gas was maintained until the vessel was sealed and following this, the vessel was placed into a preheated oven at 160°C for 5 hrs. After cooling to room temperature, the vessel was opened and the solution inside was neutralised with dropwise addition of conc. HCl. Finally, the crude product was purified by dialysis (MWCO: 1 kDa) against water for 48 hrs (water changed every 2 hrs). Final product is a colourless dispersion of Si NPs in water.

NOTA-Si NPs: NOTA-Si NPs were prepared by dispersing 1 mg of amine-terminated Si NPs in deionized water (150 μ L) in a 1.5 mL low protein binding Eppendorf-tube. The pH of the dispersion was set between 7–7.5 by 0.01 M NaOH solution. NOTA-Bn-SCN (0.1 μ mol) was dissolved in water (100 μ L) and

added to the Si NPs dispersion. The reaction was shaken on a thermomixer at 750 rpm for 16 h at 25 °C. The NOTA-Si NPs were purified by dialyzing against water (MWCO: 1 kDa). A defined aliquot of the sample was freeze-dried to obtain the concentration of particles.

IR800-Si NPs: To amine-terminated Si NPs (1 mg) dispersed in water (150 µL) at pH 7–7.5 (0.01 M NaOH), NHS-IR 800 (0.05 µmol) dissolved in water (100 µL) was added. The reaction was performed in a 1.5 mL low protein binding Eppendorf-tube in dark. The reaction mixture was shaken using a thermomixer at 750 rpm at 35 °C. The green solution starts to turn blue within 15 min. Upon completion of the reaction, the product was purified by dialysis (MWCO: 3.5–5 kDa) against Millipore water. The IR800-Si NPs were analysed by fluorescence measurements *via* RP-TLC. The sample was further purified by SEC (Sephadex G-25) with 0.9% (wt/v) NaCl as eluent, to obtain pure IR800-Si NPs. A known volume of the dispersion was lyophilized to determine the concentration of the nanoconjugate.

NOTA-IR800-Si NPs: Si NPs (1 mg) dispersed in water (500 µL) were neutralised to pH 7–7.5 (0.01 M NaOH). To this solution, 20 µL NHS-IR800 (0.05 µmol in 100 µL water) and 20 µL NOTA-Bn-SCN (0.1 µmol in 100 µL water) were added in 5 cycles over a period of 1 h. The reaction was run for 8 h at 35 °C. NOTA-IR800-Si NPs were purified by dialyzing the solution against water (MWCO: 3.5–5 kDa) followed by SEC. The concentration of the purified NP conjugate was obtained by freeze-drying a known volume of the sample.

Determination of dye concentration

The IR 800 dye concentration for IR800-Si NPs and NOTA-IR800-Si NPs was determined by UV-Vis titration. A stock solution of known concentration of IR 800 dye was prepared in Millipore water. 5 samples with increasing concentrations were prepared from the stock. Each dye sample was measured for absorbance keeping the value between 0.01–0.1 AU. A graph was plotted with this data, (absorbance vs concentration) which lead to a straight line passing through the origin. A sample with known amount of Si NP conjugates was measured for its absorbance and plotted on the same graph. The Beer-Lambert's equation was used for the determination of the amount of dye present per mg of Si NP conjugate.

Relative quantum yield determination

The photoluminescent quantum yield of the IR800 dye coupled to unimodal and bimodal Si NP conjugates was determined using free IR800 dye as a reference. The QY of free NHS-IR 800 dye according to previously published data is 14.2%. The UV-Vis absorbance of the water dispersed Si NP conjugates and free IR800 dye was measured. To minimize the re-absorption effects, the absorbance signals were always kept between 0.01–0.10 AU. The maximum absorbance (~615 nm) was used as the excitation wavelength for the fluorescence emission. A slit width of 5 mm was kept constant for all the measurements. The resulting fluorescence signal was integrated, and the quantum yield was calculated.

Radiolabelling of Si NP conjugates (NOTA-Si NPs/NOTA-IR800-Si NPs)

The production of ^{64}Cu was performed at a Cyclone®18/9 (Helmholtz-Zentrum Dresden-Rossendorf). For the $^{64}\text{Ni}(p,n)^{64}\text{Cu}$ nuclear reaction, 15 MeV protons with a beam current of 12 µA for 150 min were used. The yields of the nuclear reaction $^{64}\text{Ni}(p,n)^{64}\text{Cu}$ were 3.6–5.2 GBq [at the end of bombardment (EOB)] with molar activities of 150–250 GBq μmol^{-1} Cu diluted in HCl (10 mM).⁶⁸ An aqueous solution of [^{64}Cu]CuCl₂ (10 MBq) was added to ~0.1 mg (1 mg/mL stock solution) of NOTA-Si NPs and NOTA-IR800-Si NPs dispersed in water. 100 mM MES buffer at pH 6 was used to make the final volume up to 400 µL. The reaction mixtures were shaken at room temperature for 30 min, which resulted in RCY ~ 80–90%. The radiolabelling was monitored using Radio-iTLC.

Radiochemical analysis of the yields and kinetics of the experiments was determined using different stationary phase and eluent systems. iTLC plates were purchased from Agilent Technologies. The air-dried TLC strips were exposed to a high-resolution phosphor imaging plate (GE Healthcare). The exposed plates were scanned with an Amersham Typhoon 5 Scanner (GE Healthcare) or read by a radioluminography laser scanner BAS-1800II (Raytest). Aida Image Analyzer version 4.0 software was used for data analysis and conversion of data to ASCII before graph-plotting in Origin.

Radio-SEC was performed using PD-10 Desalting G25 columns (Sephadex, G25 medium) to purify the traces of free [^{64}Cu]CuCl₂. The ^{64}Cu -complexes were purified using water or 0.9% NaCl solution as the mobile phase. The radiochemical yields for [^{64}Cu]Cu-NOTA-Si NPs were determined to be 90–95% whereas for [^{64}Cu]Cu-NOTA-IR800-Si NPs 80–95%.

Radiometric titration to determine the amount of NOTA on Si NPs

Radiometric titrations were conducted using a mixture of radioactive $^{64}\text{Cu}(\text{II})$ and non-radioactive Cu(II) for the determination of the amount of NOTA conjugated to Si NPs. To 10 µL aliquots of the NOTA-Si NPs and NOTA-IR800-Si NPs (0.2 mM stock solution in 100 mM MES buffer, pH 5.5), known amounts of a mixture of [^{64}Cu]CuCl₂ and CuSO₄ with a final concentration of 0.4 mM (stock solution) were added. The solutions were stirred for 1 h at room temperature on a thermomixer at 750 rpm. After complete complexation (confirmed using Radio-iTLC), an 8-fold excess of EDTA was added to each solution vial to remove any non-specifically bound Cu(II) ions. The resulting solutions were stirred at 37 °C for 40 min at 750 rpm. The RCY was determined *via* Radio-iTLC and also on a Radio-SEC (Sephadex G-25). The amount of chelator per mg Si NP conjugate was calculated using the percentage of Cu(II) ions bound to the conjugate according to the equation:

$$\text{moles of chelator conjugated} = \text{moles (II)} \cdot [\% ^{64}\text{Cu(II)} (Rf < 0.2) / \% ^{64}\text{Cu (total)}]$$

The amount of NOTA conjugated to Si NPs was calculated.

***In vitro* assessment of nanotoxicity**

All biocompatibility assays were conducted as per the protocol specified in the ISO Norm 10993–5:2009. All cell culture reagents were purchased from Biochrom AG and Sigma-Aldrich unless otherwise stated. The human embryonic kidney cell lines HEK293 (DMSZ number ACC 305) were cultured in DMEM + 10% fetal calf serum (FCS) and incubated in humidified atmosphere of 95% air/ 5% CO₂ at 37°C. The cell number and the viability of the cells was determined using CASY cell counter (Roche Diagnostics) following the manufacturer's protocol. The cell lines were regularly tested and were confirmed to be mycoplasma negative using the LookOut mycoplasma PCR detection kit (Sigma-Aldrich). For the cell viability and LDH assays, the cells were treated with penicillin/streptomycin to avoid any bacterial growth during the experiments.

The *in vitro* assessment was performed using MTS (3-(4,5-dimethylthiazol-2-yl)-5-(3-carboxymethoxyphenyl)-2-(4-sulfophenyl)-2H-tetrazolium) calorimetric assay and the CyQUANT® Direct Cell Proliferation Assay. The MTS assay is based on the conversion of the tetrazolium salt to a formazan dye, presumably by NADPH and NADH produced by dehydrogenase enzymes in metabolically-active cells. The formation of the dye in the presence of the NP is monitored by optical absorbance measurement at 490 nm, and the viability is finally compared with the untreated cellular control. In addition to that, the membrane integrity was measured by an LDH assay which quantifies lactate dehydrogenase (LDH), an enzyme that is released upon cell lysis. The CyQUANT assay is a fluorescence-based proliferation and cytotoxicity assay and therefore can be used to assess cell growth, cell viability, or compound toxicity. For the evaluation of cytotoxicity, the non-cancerous cell line, HEK 293 Human epithelial kidney; was seeded in sterile 96-well microtiter plates (Greiner Bio-One) at a density of 1.8×10^4 cells per well were seeded in DMEM media and allowed to grow for 24 h prior to addition of the selected samples. CyQUANT® is a direct fluorescence-based proliferation and cytotoxicity assay consisting of a fluorescent nucleic acid stain that permeates live cells and concentrates in its nucleus. The second component is a suppresser dye that is impermeable for live cells and suppresses the green fluorescence. 100 µL of CyQuant dye was added to the wells after 24 h of incubation. The fluorescence was measured after 60 min of incubation. After 24 h incubation, increasing concentrations of NOTA-Si NP, IR800-Si NP and NOTA-IR800-Si NPs conjugates were added to the cells in triplicate. After exposure for 72 h, 20 µL of MTS (Promega) was added to the wells and incubated for 40 min. Optical densities at 492 nm were measured with a microplate reader (TECAN sunrise). The viability of cells is expressed as a percentage of viable cells grown in the absence of the NPs.

Additionally, to measure the membrane integration, an LDH assay was used in the same cell lines. For this, 2.1×10^4 cells per well were seeded in a 96 microtiter plate. After 24 h incubation, the stock solutions of the conjugates were added and incubated for 72 h. 10 µL of LDH lysis buffer (cytoscan LDH from G-biosciences) was added to the cells. Optical density

was measured at 492 nm. The percentage of LDH release was expressed as the percentage of LDH release of cells grown in the absence of NPs. The data were analysed by normalizing the absorbance from each well containing the samples to the absorbance value of the cells without any samples. As a positive control, a set of a triplicate of cells were treated with the supplied lysis buffer and the percentage of LDH release was expressed relative to this control. As a negative control, bovine serum albumin in triplicate of cells was used.

Animal experiments

***In vivo* small animal PET**

All animal experiments were carried out according to the guidelines of the German Regulations for Animal Welfare and the protocols approved by the local Ethical Committee for Animal Experiments (AZ 24-9168.21-4/2004-1, AZ 24-9168.11-4/2012-1). Animals received standard food and tap water *ad libitum* and were anesthetized prior to animal experiments using 10% desflurane in 30% oxygen/air. Male and female NMRI nu/nu mice (RjOrl:NMRI-Foxn1nu/Foxn1nu) were received from Janvier Labs (Saint-Berthevin Cedex, France). Small animal PET imaging was performed using microPET® P4 scanner (Siemens Medical Solutions, Knoxville) or NanoScanPET/CT (Mediso, Budapest). Animals were positioned on a heated bed to maintain body temperature at 37°C. Mice received 10-30 MBq (50–100 µg) of Si NP conjugates in 0.5 mL and 0.2 mL E-153, respectively, intravenously over 0.5 min into a lateral tail vein. The activity of the injection solution was measured in a dose calibrator (Isomed 2000, Dresden, Germany) cross-calibrated to the PET scanners. Attenuation correction of PET data was performed by means of a 10 min transmission scan using a rotating point source of ⁵⁷Co (microPET®) or by whole body CT (NanoScan®PET/CT). Data acquisition and reconstruction were performed as described elsewhere. Three-dimensional regions of interest (ROI) were determined within masks around different organs by thresholding PET data within these masks. ROI time activity curves (TAC) were derived from subsequent data analysis. Data were calculated as standard uptake value (SUV, SUV = activity concentration in tissue [Bq/g] × body weight [g] / injected dose [Bq]) at a certain time point *p.i.* The ROI data and TAC were further analysed using R (R is available as Free Software under the terms of the Free Software Foundation's GNU General Public License in source code form) and specially developed program packages (Jörg van den Hoff, Helmholtz-Zentrum Dresden - Rossendorf, Dresden, Germany). The data were calculated in standard uptake value (SUV, in units of grams per milliliter), defined as the tracer concentration at a certain time point normalized to injected dose per unit body weight. The SUV was used for better comparison within animals of different size and weight and with other species. The graphs were calculated with GraphPad Prism version 5.00 for Windows (GraphPad Software, San Diego California USA, www.graphpad.com).

Biodistribution studies

For biodistribution experiments, NMRI nu/nu mice were intravenously injected with ~0.5 mL 0.5-10 MBq (10-100 µg) of ⁶⁴Cu-labelled [⁶⁴Cu]Cu-NOTA-Si NPs and [⁶⁴Cu]Cu-NOTA-IR800-Si NPs. Animals were sacrificed at different time points. Organs and tissues of interest were excised, weighed, and radioactivity was determined using Wizard™3" gamma counter. Activity in selected organs and tissues was expressed as % injected dose (%ID), %ID/g tissue, or SUV. The obtained blood volume amounted to 400-500 µL. Afterwards, urine samples (200 - 400 µL) were obtained by puncture of bladder.

Optical imaging

For optical imaging experiments, anesthetized healthy NMRI nu/nu mice were intravenously injected with 20 µL IR800-Si NPs and NOTA-IR800-Si NPs (~80 µg each) respectively. Fluorescence was measured using the small animal In-vivo-Imaging System FX Pro (Carestream Health, USA) in fluorescence mode (Ex 600 nm, Em 753 nm; reference image for autofluorescence: Ex 430 nm, Em 535 nm). Fluorescence pictures were merged with the X-ray acquisitions. Afterwards, animals were sacrificed, organs and tissues of interest were excised, and fluorescence was measured again.

Conflicts of interest

There are no conflicts to declare.

Acknowledgements

We thank Utta Herzog and Karin Landrock for excellent technical assistance. Financial support by the Helmholtz Association (funding through the Helmholtz Virtual Institute NanoTracking, Agreement Number VH-VI-421) is gratefully acknowledged.

References

- 1 S. Achilefu, *Chem. Rev.*, 2010, **110**, 2575.
- 2 P. J. Cassidy and G. K. Radda, *J. R. Soc. Interface*, 2005, **2**, 133.
- 3 J. V. Frangioni, *J. Clin. Oncol.*, 2008, **26**, 4012.
- 4 M. L. James and S. S. Gambhir, *Physiol. Rev.*, 2012, **92**, 897.
- 5 G. Singh, M. D. Gott, H. J. Pietzsch and H. Stephan, *Nuklearmedizin*, 2016, **55**, 41.
- 6 R. Weissleder, *Science*, 2006, **312**, 1168.
- 7 A. Louie, *Chem. Rev.*, 2010, **110**, 3146.
- 8 B. R. Smith and S. S. Gambhir, *Chem. Rev.*, 2017, **117**, 901.
- 9 G. Chen, I. Roy, C. Yang and P. N. Prasad, *Chem. Rev.*, 2016, **116**, 2826.
- 10 B. Pelaz, S. Jaber, D. J. de Aberasturi, V. Wulf, T. Aida, J. M. de la Fuente, J. Feldmann, H. E. Gaub, L. Josephson, C. R. Kagan, N. A. Kotov, L. M. Liz-Marzán, H. Mattoussi, P. Mulvaney, C. B. Murray, A. L. Rogach, P. S. Weiss, I. Willner and W. J. Parak, *ACS Nano*, 2012, **6**, 8468.
- 11 K. L. Viola, J. Sbarboro, R. Sureka, M. De, M. A. Bicca, J. Wang, S. Vasavada, S. Satpathy, S. Wu, H. Joshi, P. T. Velasco, K. MacRenaris, E. A. Waters, C. Lu, J. Phan, P. Lacor, P. Prasad, V. P. Dravid and W. L. Klein, *Nat. Nanotechnol.*, 2015, **10**, 91.
- 12 S. Marchesan and M. Prato, *ACS Med. Chem. Lett.*, 2013, **4**, 147.
- 13 O. S. Wolfbeis, *Chem. Soc. Rev.*, 2015, **44**, 4743.
- 14 B. Pelaz, C. Alexiou, R. A. Alvarez-Puebla, F. Alves, A. M. Andrews, S. Ashraf, L. P. Balogh, L. Ballerini, A. Bestetti, C. Brendel, S. Bosi, M. Carril, W. C. W. Chan, C. Chen, X. Chen, X. Chen, Z. Cheng, D. Cui, J. Du, C. Dullin, A. Escudero, N. Feliu, M. Gao, M. George, Y. Gogotsi, A. Grünweller, Z. Gu, N. J. Halas, N. Hampf, R. K. Hartmann, M. C. Hersam, P. Hunziker, J. Jian, X. Jiang, P. Jungebluth, P. Kadhiresan, K. Kataoka, A. Khademhosseini, J. Kopeček, N. A. Kotov, H. F. Krug, D. S. Lee, C.-M. Lehr, K. W. Leong, X.-J. Liang, M. Ling Lim, L. M. Liz-Marzán, X. Ma, P. Macchiaroni, H. Meng, H. Möhwald, P. Mulvaney, A. E. Nel, S. Nie, P. Nordlander, T. Okano, J. Oliveira, T. H. Park, R. M. Penner, M. Prato, V. Puntès, V. M. Rotello, A. Samarakoon, R. E. Schaak, Y. Shen, S. Sjöqvist, A. G. Skirtach, M. G. Soliman, M. M. Stevens, H.-W. Sung, B. Z. Tang, R. Tietze, B. N. Udugama, J. S. VanEpps, T. Weil, P. S. Weiss, I. Willner, Y. Wu, L. Yang, Z. Yue, Q. Zhang, Q. Zhang, X.-E. Zhang, Y. Zhao, X. Zhou and W. J. Parak, *ACS Nano*, 2017, **11**, 2313.
- 15 S. Kunjachan, J. Ehling, G. Storm, F. Kiessling and T. Lammers, *Chem. Rev.*, 2015, **115**, 10907.
- 16 J. A. Barreto, W. O'Malley, M. Kubeil, B. Graham, H. Stephan and L. Spiccia, *Adv. Mat.*, 2011, **23**, H18.
- 17 M. Longmire, P. L. Choyke and H. Kobayashi, *Nanomedicine (London, England)*, 2008, **3**, 703.
- 18 K. Zarschler, L. Rocks, N. Licciardello, L. Boselli, E. Polo, K. P. Garcia, L. De Cola, H. Stephan and K. A. Dawson, *Nanomedicine: NBM*, 2016, **12**, 1663.
- 19 L. A. Kunz-Schughart, A. Dubrovskaya, C. Peitzsch, A. Ewe, A. Aigner, S. Schellenburg, M. H. Muders, S. Hampel, G. Cirillo, F. Iemma, R. Tietze, C. Alexiou, H. Stephan, K. Zarschler, O. Vittorio, M. Kavallaris, W. J. Parak, L. Madler and S. Pokhrel, *Biomaterials*, 2017, **120**, 155.
- 20 X. Jiang, B. Du, Y. Huang and J. Zheng, *Nano Today*, 2018, **21**, 106.
- 21 J. Joo, X. Liu, V. R. Kotamraju, E. Ruoslahti, Y. Nam and M. J. Sailor, *ACS Nano*, 2015, **9**, 6233.
- 22 J.-H. Park, L. Gu, G. von Maltzahn, E. Ruoslahti, S. N. Bhatia and M. J. Sailor, *Nat. Mater.*, 2009, **8**, 331.
- 23 M. Rosso-Vasic, E. Spruijt, Z. Popovic, K. Overgaag, B. van Lagen, B. Grandidier, D. Vanmaekelbergh, D. Dominguez-Gutierrez, L. De Cola and H. Zuilhof, *J. Mater. Chem.*, 2009, **19**, 5926.
- 24 X. Cheng, S. B. Lowe, P. J. Reece and J. J. Gooding, *Chem. Soc. Rev.*, 2014, **43**, 2680.
- 25 J. H. Warner, A. Hoshino, K. Yamamoto and R. D. Tilley, *Angew. Chem. Int. Ed. Engl.*, 2005, **44**, 4550.
- 26 X. Cheng, S. B. Lowe, S. Ciampi, A. Magenau, K. Gaus, P. J. Reece and J. J. Gooding, *Langmuir*, 2014, **30**, 5209.
- 27 C. M. Hessel, M. R. Rasch, J. L. Hueso, B. W. Goodfellow, V. A. Akhavan, P. Puvanakrishnan, J. W. Tunnel and B. A. Korgel, *Small*, 2010, **6**, 2026.
- 28 Y. He, Y. Zhong, F. Peng, X. Wei, Y. Su, Y. Lu, S. Su, W. Gu, L. Liao and S.-T. Lee, *J. Am. Chem. Soc.*, 2011, **133**, 14192.
- 29 C. Song, Y. Zhong, X. Jiang, F. Peng, Y. Lu, X. Ji, Y. Su and Y. He, *Anal. Chem.*, 2015, **87**, 6718.

- 30 F. Erogbogbo, K.-T. Yong, I. Roy, G. Xu, P. N. Prasad and M. T. Swihart, *ACS Nano*, 2008, **2**, 873.
- 31 Y. He, Y. Su, X. Yang, Z. Kang, T. Xu, R. Zhang, C. Fan and S.-T. Lee, *J. Am. Chem. Soc.*, 2009, **131**, 4434.
- 32 Y. Zhong, F. Peng, X. Wei, Y. Zhou, J. Wang, X. Jiang, Y. Su, S. Su, S.-T. Lee and Y. He, *Angew. Chem. Int. Ed. Engl.*, 2012, **51**, 8485.
- 33 Y. Zhong, F. Peng, F. Bao, S. Wang, X. Ji, L. Yang, Y. Su, S.-T. Lee and Y. He, *J. Am. Chem. Soc.*, 2013, **135**, 8350.
- 34 L. Ruizendaal, S. P. Pujari, V. Gevaerts, J. M. Paulusse and H. Zuilhof, *Chemistry, an Asian journal*, 2011, **6**, 2776.
- 35 L. Wang, V. Reipa and J. Blasic, *Bioconjug. Chem.*, 2004, **15**, 409.
- 36 R. Intartaglia, A. Barchanski, K. Bagga, A. Genovese, G. Das, P. Wagener, E. Di Fabrizio, A. Diaspro, F. Brandi and S. Barcikowski, *Nanoscale*, 2012, **4**, 1271.
- 37 F. Erogbogbo and M. T. Swihart, ENEA Res Ctr Frascati, Rome, ITALY, 2010.
- 38 J. H. Ahire, M. Behray, C. A. Webster, Q. Wang, V. Sherwood, N. Saengkrit, U. Ruktanonchai, N. Woramongkolchai and Y. Chao, *Adv. Healthc. Mat.*, 2015, **4**, 1877.
- 39 C.-H. Lai, J. Hütter, C.-W. Hsu, H. Tanaka, S. Varela-Aramburu, L. De Cola, B. Lepenies and P. H. Seeberger, *Nano Lett.*, 2016, **16**, 807.
- 40 Z. F. Li and E. Ruckenstein, *Nano Lett.*, 2004, **4**, 1463.
- 41 J. H. Warner, A. Hoshino, K. Yamamoto and R. D. Tilley, *Angew. Chem. Int. Ed. Engl.*, 2005, **44**, 4550.
- 42 S. Ohta, P. Shen, S. Inasawa and Y. Yamaguchi, *J. Mater. Chem.*, 2012, **22**, 10631.
- 43 L. Ruizendaal, S. Bhattacharjee, K. Pournazari, M. Rosso-Vasic, L. H. J. de Haan, G. M. Alink, A. T. M. Marcelis and H. Zuilhof, *Nanotoxicology*, 2009, **3**, 339.
- 44 S. Bhattacharjee, I. M. Rietjens, M. P. Singh, T. M. Atkins, T. K. Purkait, Z. Xu, S. Regli, A. Shukaliak, R. J. Clark, B. S. Mitchell, G. M. Alink, A. T. Marcelis, M. J. Fink, J. G. Veinot, S. M. Kauzlarich and H. Zuilhof, *Nanoscale*, 2013, **5**, 4870.
- 45 S. Bhattacharjee, L. de Haan, N. Evers, X. Jiang, A. Marcelis, H. Zuilhof, I. Rietjens and G. Alink, *Part. Fibre Toxicol.*, 2010, **7**, 1.
- 46 M. Dasog, Z. Yang, S. Regli, T. M. Atkins, A. Faramus, M. P. Singh, E. Muthuswamy, S. M. Kauzlarich, R. D. Tilley and J. G. C. Veinot, *ACS Nano*, 2013, **7**, 2676.
- 47 Q. Li, T. Y. Luo, M. Zhou, H. Abroshan, J. Huang, H. J. Kim, N. L. Rosi, Z. Shao and R. Jin, *ACS Nano*, 2016, **10**, 8385.
- 48 X. Chen, X. Zhang, L. Y. Xia, H. Y. Wang, Z. Chen and F. G. Wu, *Nano Lett.*, 2018, **18**, 1159.
- 49 X. Cheng, E. Hinde, D. M. Owen, S. B. Lowe, P. J. Reece, K. Gaus and J. J. Gooding, *Adv. Mater.*, 2015, **27**, 6144.
- 50 B. F. P. McVey, D. Konig, X. Cheng, P. B. O'Mara, P. Seal, X. Tan, H. A. Tahini, S. C. Smith, J. J. Gooding and R. D. Tilley, *Nanoscale*, 2018, **10**, 15600.
- 51 F. Erogbogbo, K. T. Yong, I. Roy, R. Hu, W. C. Law, W. Zhao, H. Ding, F. Wu, R. Kumar, M. T. Swihart and P. N. Prasad, *ACS Nano*, 2011, **5**, 413.
- 52 M. P. Singh, T. M. Atkins, E. Muthuswamy, S. Kamali, C. Tu, A. Y. Louie and S. M. Kauzlarich, *ACS Nano*, 2012, **6**, 5596.
- 53 C. Tu, X. Ma, P. Pantazis, S. M. Kauzlarich and A. Y. Louie, *J. Am. Chem. Soc.*, 2010, **132**, 2016.
- 54 S. Wu, Y. Zhong, Y. Zhou, B. Song, B. Chu, X. Ji, Y. Wu, Y. Su and Y. He, *J. Am. Chem. Soc.*, 2015, **137**, 14726.
- 55 M. Qiu, A. Singh, D. Wang, J. L. Qu, M. Swihart, H. Zhang and P. N. Prasad, *Nano Today*, 2019, **25**, 135.
- 56 C. Tu, X. Ma, A. House, S. M. Kauzlarich and A. Y. Louie, *ACS Med. Chem. Lett.*, 2011, **2**, 285.
- 57 N. Licciardello, S. Hunoldt, R. Bergmann, G. Singh, C. Mamat, A. Faramus, J. L. Z. Ddungu, S. Silvestrini, M. Maggini, L. De Cola and H. Stephan, *Nanoscale*, 2018, **10**, 9880.
- 58 J. B. Wacker, I. Lignos, V. K. Parashar and M. A. M. Gijs, *Lab on a Chip*, 2012, **12**, 3111.
- 59 P. A.-O. Debie, J. Van Quathem, I. Hansen, G. Bala, S. Massa, N. Devoogdt, C. Xavier and S. Hernot, *Mol. Pharm.*, 2017, **14**, 1145.
- 60 K. P. Conner, B. M. Rock, G. K. Kwon, J. P. Balthasar, L. Abuqayyas, L. C. Wienkers and D. A. Rock, *Drug Metab. Dispos.*, 2014, **42**, 1906.
- 61 K. Pant, D. Gröger, R. Bergmann, J. Pietzsch, J. Steinbach, B. Graham, L. Spiccia, F. Berthon, B. Czarny, L. Devel, V. Dive, H. Stephan and R. Haag, *Bioconjug. Chem.*, 2015, **26**, 906.
- 62 A. Eisfeld and J. S. Briggs, *Chem. Phys.*, 2006, **324**, 376.
- 63 N. Ryu, Y. Okazaki, E. Pouget, M. Takafuji, S. Nagaoka, H. Ihara and R. Oda, *Chem. Comm.*, 2017, **53**, 8870.
- 64 S. Zhang, M. Shao P Fau - Bai and M. Bai, *Bioconjug. Chem.*, 2013, **24**, 1907.
- 65 J. H. Ahire, P. R. Wang Q Fau - Coxon, G. Coxon Pr Fau - Malhotra, R. Malhotra G Fau - Brydson, R. Brydson R Fau - Chen, Y. Chen R Fau - Chao and Y. Chao, *ACS Appl. Mater. Interfaces*, 2012, **4**, 3285.
- 66 M. Behray, C. A. Webster, S. Pereira, P. Ghosh, S. Krishnamurthy, W. T. Al-Jamal and Y. Chao, *ACS Appl. Mater. Interfaces*, 2016, **8**, 8908.
- 67 A. Z. Ruiz, D. Brühwiler, T. Ban and G. Calzaferri, *Monatshefte für Chemie / Chemical Monthly*, 2005, **136**, 77.
- 68 S. Thieme, M. Walther, H. J. Pietzsch, J. Henniger, S. Preusche, P. Mading and J. Steinbach, *Appl. Radiat. Isot.*, 2012, **70**, 602.

Table of Content

